2023 IEEE International Conference on Robotics and Automation (ICRA 2023)
May 29 - June 2, 2023. London, UK

Exploring Robot-Assisted Optical Coherence Elastography for Surgical Palpation

Yeonhee Chang[1], Elan Z. Ahronovich[2], Nabil Simaan[2†], and Cheol Song[1†]

Abstract— **Optical Coherence Elastography (OCE) is a method that discerns local tissue stiffness using optical information. This method has recently been explored for laryngeal cancer tumor margin detection but has not been widely deployed clinically. Part of the challenge hindering such clinical deployment is the need for controlled high-precision mechanical probing of the tissue. This paper explores the concept of robot-assisted optical coherence elastography(OCE) and presents a preliminary system integration used to demonstrate the approach for stiffness mapping and discerning tumor margins. The approach is demonstrated on a custom Cartesian stage robot, and a custom-built OCE system comprised of an 830 nm broad-band laser with a vector-analysis method for phase gradient estimation and strain imaging. The paper illustrates one of the advantages of robot-controlled probing in terms of increasing the accuracy of the OCE system in a large range of displacement and strain. By leveraging motion information from the robot, online re-calibration of the OCE strain map may be achieved, thereby reducing OCE errors. After calibration, it is shown that the error in estimating the local Young's modulus is 0.485% in the silicon phantom and 0.531% in the agar phantom. These results suggest that future integration of optical coherence tomography(OCT) in clinically deployable robots may offer advantages in enabling local stiffness map estimation using OCE.**

I. Introduction

Palpation of underlying anatomy during open surgery is used to detect cysts, nerve bundles, arteries, and tumors. The use of this sensory modality has been significantly hampered by the deployment of minimally invasive robot-assisted surgical systems, which do not support high-fidelity force feedback sufficient for conveying stiffness information to the surgeon [1]. Researchers in the past two decades have spent significant efforts on exploring the utility of tools for stiffness imaging in lieu of digital palpation. Examples include works on mechanical probing [2], tactile array imaging [3–5], the development of local stiffness palpation probes [6], [7], and the coupled use of ultrasound with palpation to improve tumor margin detection [8]. Many works (e.g., [9–11]) investigated the utility of stiffness information displays for assisting situational awareness in localizing anatomical features.

† Corresponding author
[1]Department of Robotics and Mechatronics Engineering, DGIST, Daegu 42988, South Korea (nyouimon, csong)@dgist.ac.kr
[2]Department of Mechanical Engineering, Vanderbilt University, Nashville, TN 37235, USA (elan.z.ahronovich, nabil.simaan)@vanderbilt.edu
*This work was supported by the DGIST R&D Program of the Ministry of Science and ICT (22-RT-01). Y. Chang were supported by 2021 DGIST Post-Graduate Research Abroad Awards.

While these technologies and methods are suitable for the detection of stiffness gradients for large tumor detection, they are not suitable for the detection of local sub-mucosal tumors, as in Laryngeal cancer, since the anatomy is very soft. Laryngeal cancer affects the main organ responsible for critical functions of breathing, swallowing, and phonation [12]. Part of the challenge in the early detection of these tumors is that they are not easily visible using white-light vision. Recently, there has been an interest in the Otolaryngeal community in exploring the feasibility of using OCT for tissue exploration and for local stiffness imaging to enable the early detection of tumor onset. Examples of works that explored the utility of OCT for laryngeal cancer include [13–15].

Despite these works, to date, there are no robotic systems deploying intracavitary OCE. In [16], the feasibility of inducing micro-motion control using continuum robots was used for 3D OCT imaging. Inspired by this work, we envision that those future systems will take advantage of highly dexterous continuum robots and OCT to achieve the goal of localized OCE imaging. This paper presents the first step towards this eventual goal with the aim of clarifying some of the advantages of using information from the robot to assist in the process of OCE imaging and stiffness estimation.

The contribution of this paper is in offering the first exploration of robot-assisted OCE with the aim of leveraging information from both of these technologies to achieve a stiffness map. We leverage motion and force information from the robot in support of the OCE imaging process. The robot-assisted OCE system has a larger measurable range of displacement and strain than the wave-based OCE approaches, which rely on shear strain estimation. Previous phase-sensitive OCE approaches require heavy computational phase unwrapping procedures for a large deformation, which can be easily corrupted [17], [18]. In this work, we only need to estimate the OCT phase shift without any unwrapping process. To produce the phase-assisted strain map, we used the vector method introduced in [19], and we then used information from the robot motion to estimate Young's modulus.

II. System Design and Method

A. Optical coherence elastography system

The OCE visualizes the stiffness of samples based on optical coherence tomographic images. It estimates elasticity change by monitoring the scatterer's movement on the OCT image according to sample excitation. There are two ways to analyze tissue stiffness in OCE. The first method is to

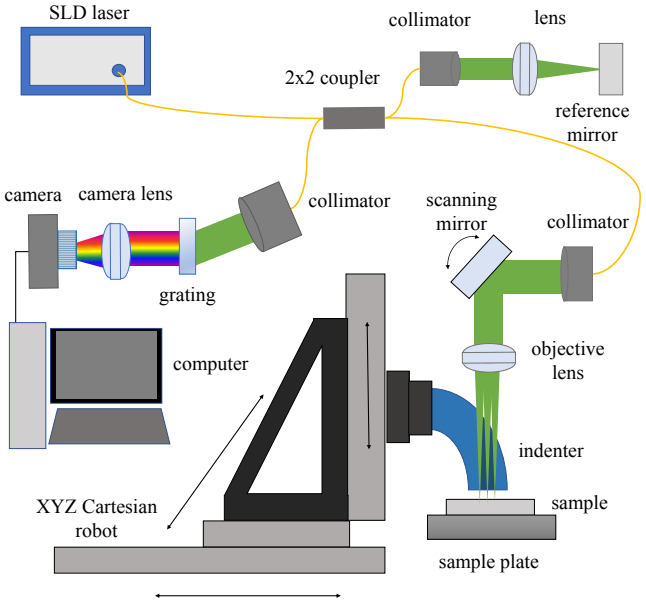

Fig. 1. Schematic diagram of the custom-built robot-assisted OCE. OCT system has a broad-band SLD laser with a center wavelength of 830 nm, a reference mirror, and a homebuilt spectrometer. The OCT system acquires a tomographic image of the sample surface. The XYZ cartesian robot is used to push down the sample surface with the indenter probe.

analyze the wave equation of a surface wave (e.g., shear wave). This method is a useful for non-contact scenarios [20], [21]; however, its measurable strain and stress range are narrow. The other method is called compression OCE [22], where scatterers' displacement along the depth direction is used to calculate strain. This method is relatively simple and can estimate a larger range of displacement and strain than what is possible with the wave equation methods. Also, the compression OCE method is appropriate for our proposed application because it can be implemented with a surgical robot for palpation.

The relationship between strain, ε_{ij}, and stress, σ_{ij}, in an isotropic medium with linear-elastic deformation as represented in [23] is:

$$\sigma_{ij} = \frac{E}{(1+\nu)}(\varepsilon_{ij} + \frac{\nu}{1-2\nu}\varepsilon_{rr}\delta_{ij}), \delta_{ij} = \begin{cases} 1, & i = j, \\ 0, & i \neq j. \end{cases} \quad (1)$$

where E is Young's modulus, and ν is Poisson's ratio. Also, the summation strain over the r index($\varepsilon_{rr}, r = 1, 2, 3$) is assumed. The ε_{ij} is considered partial differentiation of displacement when displacement is small.

$$\varepsilon_{ij} = \frac{1}{2}\left(\frac{\partial u_i}{\partial x_i} + \frac{\partial u_j}{\partial x_j}\right) \quad (2)$$

Poisson's ratio of soft tissue is about 1/2 because soft tissue is incompressible [20]. Equation (1) for uni-axial direction can be simplified:

$$\sigma_{11} = E\varepsilon_{11} \quad (3)$$

Here, when uniform stress is applied to the sample by a robot, the strain shows the mechanical properties of the sample.

In the uni-axial compression and displacement, local strain is expressed as partial differentiation of displacement as:

$$\varepsilon_{11} = \frac{\partial u_1}{\partial x_1} \quad (4)$$

Therefore, it is important to calculate the accurate displacement along the depth in OCE. The methods of calculating the scatter's displacement include calculating the cross-correlation to predict the scatter's movement and displacement through phase changes between images. In the correlation method [24–26], decorrelation occurs due to a change in the shape of a scatter, so it is difficult to obtain an accurate result and requires a long computation time. Here, analyzing the phase information [27] is more appropriate to confirm the displacement results in a short time at the surgical site. The OCT signal is represented as a complex number:

$$A\exp^{i\phi} = Acos(\phi) + iAsin(\phi) \quad (5)$$

Where A is an intensity and ϕ is a phase value. The following equation expresses the relationship between axial displacement, u, and phase gap:

$$u = \frac{\lambda_0 \Delta\phi}{4\pi n} \quad (6)$$

λ_0 is the central wavelength of the laser source, $\Delta\phi$ is the phase gap, and n is the refractive index. According to (4) and (6), the strain can be acquired from phase change.

B. Design of Robot-Assisted OCE System

Fig. 1 shows the schematic diagram of the custom-built robot-assisted OCE system. The SD-OCT system for OCE [28] uses a broad-band laser source (Broadlighter D830-HP1, Superlum Ireland) as a light source and adopts a spectrometer for detecting and processing a spectral interference signal. The laser source emits a laser with an 830 nm central wavelength and a bandwidth of 70 nm. The Laser source goes to a sample arm and reference arm through a 2 x 2 coupler [29]. Galvano mirror scans the sample's surface to make the 2D image (Thorlabs). The spectral interference between the reference beam and the back-reflected beam from the sample occurs in the coupler, and the interference signal is detected by a custom spectrometer. The spectrometer is composed of a volume holographic phase transmission grating (1200 line/mm @840 nm, Wasatch Photonics), a three-element air-spaced camera lens (f=120 mm), and a line CCD camera (10-bit, Basler). The camera has 2048 elements, and the size of each element is 10 µm x 10 µm. A frame grabber board (PCI Express 1427, National Instruments) transfers the acquired image data into to personal computer.

The robotic system is a custom Cartesian stage robot with a six-degree of freedom (DoF) force/torque (FT) sensor (ATI Gamma, ATI Industrial Automation, Apex, NC, USA) attached to the end effector [10]. The Cartesian robot is constructed with three mutually orthogonal ballscrew-driven

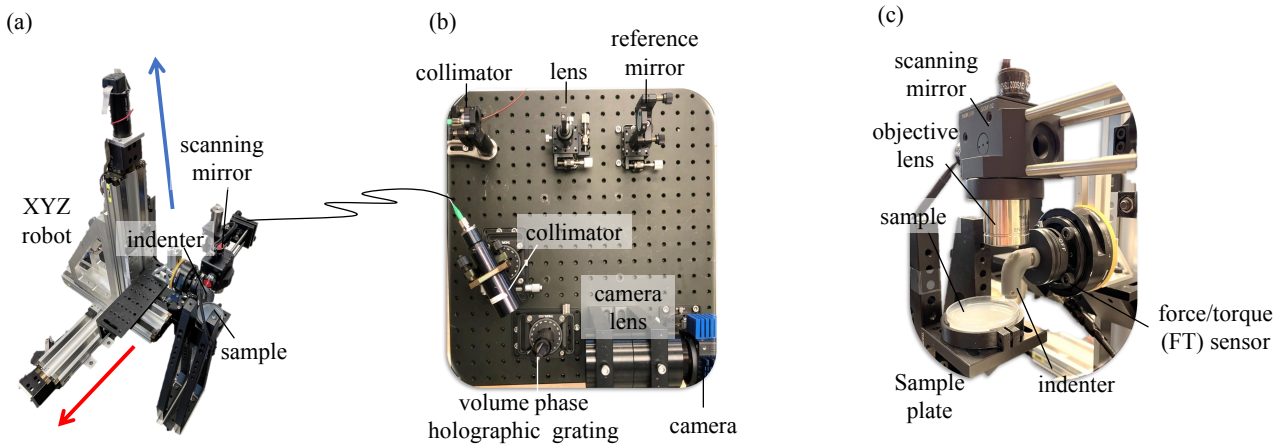

Fig. 2. Implementation of the custom-built robot-assisted OCE. (a) a XYZ Cartesian stage robot. The robot system moves in x and y directions to align the indenter and the OCT scanning head. Also, it moves z direction to push down the indenter. (b) a custom-built SD-OCT. The OCT system measures the displacement of the sample according to the indentation. (c) an indenter probe, including a force/torque sensor. The indenter probe has a slit as an OCT imaging window, and a force/torque sensor is used to measure force to estimate Young's modulus of the sample.

Parker$^{\text{TM}}$ 404XR series linear stages with 200 mm stroke. Each stage is actuated with a 90 Watt brushed DC motor (Maxon$^{\text{TM}}$ RE35 #273754) equipped with a 1000 count-per-turn encoder (Avago HEDM 5540 B11). The system is controlled using a Simulink Real Time target computer running the low-level computed torque control loop. The target machine's sample frequency is running at 1 kHz, and the force sensor measurements are filtered using a moving average filter with a window size of 40 to give a force sampling frequency of 25 Hz.

C. Implementation of Robot-Assisted OCE System

Fig. 2 shows the implemented configuration of a robot-assisted OCE system consisting of an OCT imaging component and a robotic mechanical indentation component. Fig. 2(a) shows a custom Cartesian stage robot. The SD-OCT system for the OCE is shown in Fig.2(b), and the SD-OCT system is explained in Section II-B. Fig. 2(c) shows a plastic probe mounted to the FT sensor for sample indentation with a channel to allow unobstructed pass-through of the OCT scan beam. Considering Young's modulus of soft tissue, the measurable elastic modulus is 8 MPa. The measurable Young's modulus range determined the contact surface. Young's modulus of typical soft tissue is from 1 kPa to 5 MPa. The maximum measurable elastic modulus is set as 8 Mpa by considering soft tissue Young's modulus. The sample thickness is assumed as $\sim$ 3 mm, and the displacement range is from 10 um to 100 um. As a result, the measurable strain range is from 0.0033 to 0.03. The torque/force sensor can measure 0.005 N $\sim$ 18 N. Therefore, the contacting area of the indenter should be 75 mm^2 to make the maximum measurable Yong's modulus of 8 MPa. A radial slit of 150 μm as an imaging window is located in the center of the contact area. The width of the slit should be narrow enough to prevent the sample surface from swelling.

D. Compression Optical Coherence Elastography Algorithms

Fig. 3 shows the signal analysis process to obtain a sample's strain. The spectrometer of the SD-OCT system obtains the raw spectrum. This spectrum at the wavelength domain was converted to a k-domain signal via k-linearization. A fast Fourier transform (FFT) was performed to obtain frequency information related to the depth. Next, a phase difference between the reference and deformed images is acquired. Since the phase represents only $-\pi$ to $+\pi$, the maximum phase gap, $\Delta\phi$ is 2π. In this case, according to (6), the deformation that can be measured in air (n = 1) is 0.412 μm when 0.83 μm of the central wavelength laser source is used. Therefore, the accurate displacement cannot be calculated when the displacement is 0.412 μm or more. Least-square methods [30], vector methods [19], and deep learning method [31] have been suggested to overcome small measurable displacements. For this work, vector analysis was used because it has the potential to achieve real-time calibration and strain analysis.

The vector analysis uses the real and imaginary terms of the OCT signals. The pixel intensity and phase are considered as the length and angle of the vector on the complex plane, respectively, and the phase change is expressed as an angle change of vector summation. The vector analysis method is shown in Fig. 3. First, to obtain the phase gap from the pixel index (x,z), we multiply the conjugated signal from a reference image, $a_r(x,z)$, and the signal from a deformed image, $a_d(x,z)$, of the pixel index:

$$b(x,z) = B(x,z)\exp^{i\Delta\phi(x,z)} = a_d(x,z)a_r(x,z)^* \quad (7)$$

The averaging with a 3 x 3 window size is conducted to get a homogeneous value in the iso-phase line. The values in the window are summed to average:

$$\bar{b}(x,z) = \sum_{p=x}^{x+2}\sum_{q=z}^{y+2} b(p,q) \quad (8)$$

The next step is to find the pixel gradient in a depth direction. The inter-pixel phase change in depth is calculated from (9):

$$d(x,z) = \bar{b}(x,z+\alpha)\bar{b}(x,z)^* \tag{9}$$

where z is the current pixel index in-depth, and α is the number of pixel intervals. We use $\alpha = 1$ for this study. The summation in 16 x 16 ROI along the image scan is achieved to reduce inhomogeneity and incorrect displacement estimation from the decorrelation of the optical phase caused by straining in compression OCE.

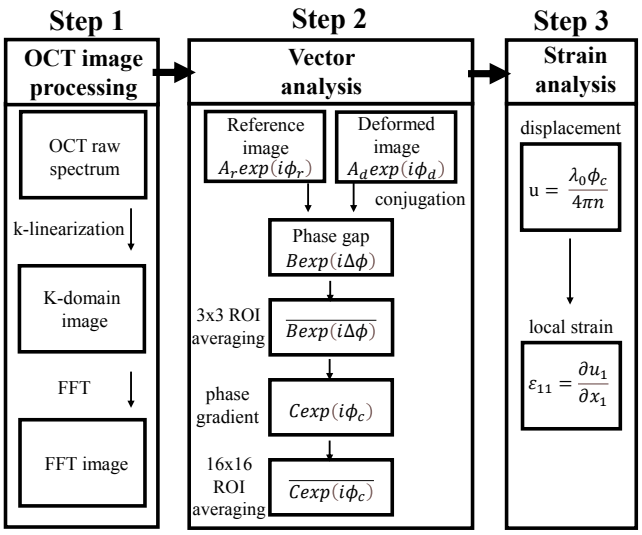

Fig. 3. Vector method based OCE signal processing. The final results of each step are used as raw data for the next step.

E. OCE calibration

The experiment protocol to measure the sample's strain is as follows; first, the sample is set on the sample plate under the OCT scan head. Next, the slit window in the palpation probe, and OCT scanning area are aligned on the XY plane. The indenter probe is moved to its initial depth. The step size of each depth increment was 15 μm. The initial OCT image is saved before the deformation and the probe is moved to another depth. The deformed OCT image is saved, and the strain is calculated based on the phase gap between acquired OCT images and corrected with calibration parameters.

The strain of depth, ($\varepsilon_{oce}(d)$), is calculated by adding up the strain at all previous locations.

$$\varepsilon_{oce}(d) = \sum_{j=1}^{n} \breve{\varepsilon}_{oce}(j) \tag{10}$$

where $\breve{\varepsilon}_{oce}(j)$ is the strain calculated at step increment j. Note that this is a change in strain based on the current and previous indentation depth. Therefore, the total strain is the sum of the incremental strains measured by the OCE for each small indentation depth increment.

The strain estimated from force and motion measurement by the robot, ($\varepsilon_r(d)$), could be expressed as a linear system, and the corrected OCE strain($\tilde{\varepsilon}_{oce}$) should match the reference strain as obtained by the robot.

$$\tilde{\varepsilon}_{oce}(d) = \mu\varepsilon_{oce}(d) + \nu = \varepsilon_r(d) \tag{11}$$

where μ and ν are calibration parameters that can be periodically re-estimated in batch mode using the robot strain information in the last k steps. Equation (11) for the last k depths can be expressed as:

$$\underbrace{\begin{bmatrix} \varepsilon_{oce}(d_1) & 1 \\ \varepsilon_{oce}(d_2) & 1 \\ \vdots & \vdots \\ \varepsilon_{oce}(d_k) & 1 \end{bmatrix}}_{\mathbf{A}} \underbrace{\begin{bmatrix} \mu \\ \nu \end{bmatrix}}_{\mathbf{c}} = \underbrace{\begin{bmatrix} \varepsilon_r(d_1) \\ \varepsilon_r(d_2) \\ \vdots \\ \varepsilon_r(d_k) \end{bmatrix}}_{\boldsymbol{\epsilon}} \tag{12}$$

The OCE calibration parameters can be solved by using:

$$\mathbf{c} = \mathbf{A}^{\dagger}\boldsymbol{\epsilon} \tag{13}$$

The above approach might confuse readers to conclude that using the OCE may not be needed since we can obtain this information from a robot equipped with an F/T sensor. However, the OCE algorithm presented above needs to be calibrated once. The experimental section below shows that this approach works reasonably well even if the tissue model being palpated is changed. Therefore, the OCE approach may still be useful if a surgical robot has integrated OCT in its tip but no accurate force and motion sensing. Suppose the robot has integrated an F/T sensor at its tip. Instead of the above naïve batch estimation approach, one may use a linear recursive estimation framework in batch mode or a Kalman filtering framework to re-calibrate the OCE. Finally, the OCE sensory modality can provide *local strain* information that is not perceptible using the robot with an F/T sensor at its tip.

III. Experiment

A. Phantom fabrication

A 3.5 mm thick silicon phantom was used for the feasibility tests. Dragon Skin™10 Fast (Smooth-On, Inc., PA), with a 10A shore modulus, was used to prepare the phantom in a petri dish. The sample was degassed in a vacuum chamber for approximately 5 minutes to ensure homogeneity. A 6mm thick agar phantom was also used for the calibration and feasibility test. 2.4 g of agar powder (Sigma-Aldrich) was dissolved in distilled water and boiled on a hot plate. Since agar is not naturally OCT opaque, 2.4 g of powder coffee creamer was added to the solution [32]. The amount of coffee creamer was determined as the best for image quality through experiments.

B. Calibration experiment results

The estimated displacement only by the phase-sensitive OCE system, uncalibrated OCE is different from the robot displacement due to the signal-to-noise ratio limit of the OCT system and errors in the vector-based strain estimation method. Since the silicon phantom is not perfectly homogeneous, isotropic, or linearly elastic, the OCE strain should be calibrated to the reference estimation of the robotic system. The OCT images were acquired at fourteen different depths.

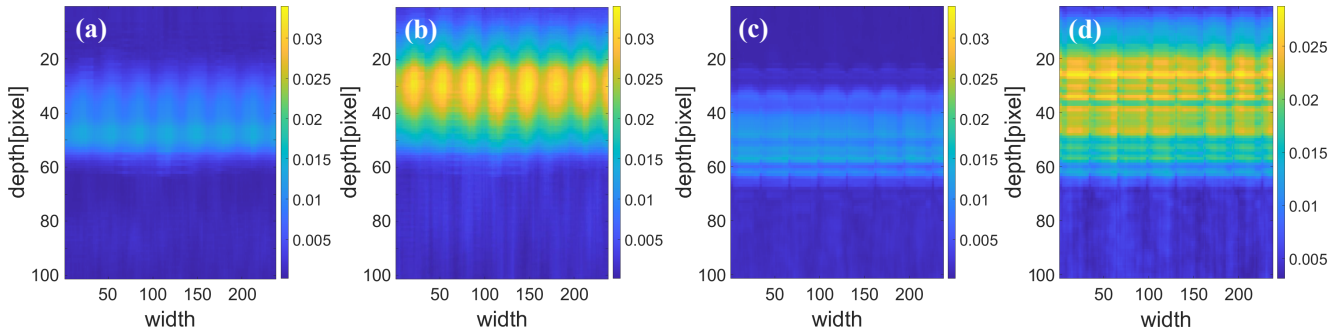

Fig. 4. Strain maps at different indentation depths. (a),(b) strain map from silicon phantom for calibration, (c),(d) strain map from agar phantom for calibration. (a) and (c) are strain maps from the third indentation depth, and (b) and (d) are the results of the final indentation depth.

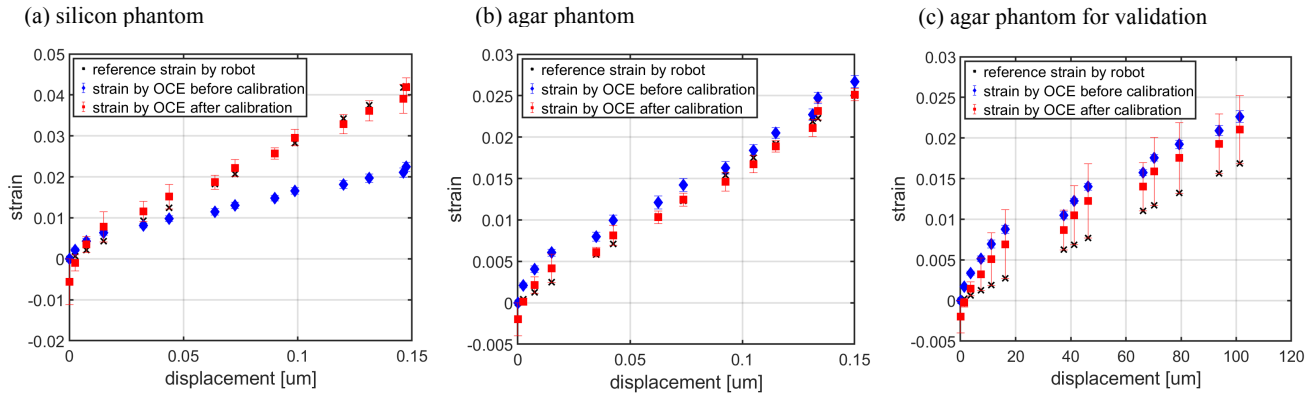

Fig. 5. The estimated strain of phantoms before and after calibration (a) silicon phantom, (b) agar phantom, and (c) second agar phantom results. The strain of (c) is calibrated with the calibration parameter from (b).

For strain calculations, we used a mean displacement between each depth. We used three images acquired at a given depth to estimate the strain map. The displacements between every step were calculated in OCE because the meaningful phase gaps could not be calculated when the displacement was large. Fig. 4 shows strain maps of phantoms. (a) and (b) are the silicon phantom results, and (c) and (d) are the agar phantom results.

Fig. 5(a) shows the calibration results of the silicon phantom's strain estimation before and after calibration. The black cross is a reference strain from the XYZ Cartesian robot, and the blue diamonds are only phase-sensitive OCE results by the vector method. Red squares are corrected strain along the displacement by the Robot-assisted OCE with the calibration parameters. In this experiment, the resultant calibration parameters are $\mu = 2.121$ and $\nu =$ -0.0056. The strain measured in the silicon phantom experiment by the robot was 0.0421, and the estimated OCE strain before calibration was 0.0224. After calibration, the re-calculated OCE strain is 0.0419, and the root-mean-square-error (RMSE) between strain from the robot and OCE after calibration is 0.0026. The force measured by the load cell is 0.147 N, corresponding to the silicon phantom's Young modulus of 0.418 MPa.

Fig. 5(b)shows the agar phantom's strain estimation results before and after calibration. The calibration parameters of the agar phantom are $\mu = 1.0167$ and $\nu =$ -0.002. In the agar phantom experiment, the total strain measured by the robot was 0.025. The total strain estimated by OCE is 0.0267 before calibration and 0.0251 after calibration. The RMSE between the reference strain from the robot and the estimated OCE stain after calibration is 0.001. The measured force in the agar phantom test was 0.331 N, with the resultant Young's modulus of the phantom as 0.162 MPa.

To evaluate the OCE error across a different palpation sample, we fabricated a second agar model and repeated the data collection using the robot and the calibrated OCE data based on the first agar phantom that was used for OCE parameter calibration. Fig. 5(c) shows the results for the OCE and robot strain information. These results show the maximal error at full scale in 19.7%, which explains why we believe that the OCE may be calibrated only periodically using robot information. These results show that the calibration with the robot system helps to improve the accuracy of strain by the OCE system.

IV. Discussion

In the case of phase-sensitive compression OCE, it is possible to estimate the strain change along the depth direction in the tomography images. Our results suggest that the OCE

method can benefit from batch calibration from robot data. Also, it was shown that one-time calibration can still hold for a different sample of agar without having to re-run the calibration. We showed that the error in estimating Young's modulus for a different sample without an update of the OCE calibration parameters was less than 20%. We believe that the exact values of Young's modulus are less important than the ability to discern spatial gradients in Young's modulus. Therefore, we believe that these results suggest that using OCE for tumor localization will be possible using our approach.

The expected shore modulus of the silicon phantom provided by the silicon material manufacturer is 10A, and the range of Young's modulus of agar phantom is 1.3 kPa for 1% of agar phantom to 3.0 MPa for 10% agar phantom [33]. Our OCE method measured Young's modulus to be 0.418 MPa and 0.162 MPa for the silicon and the agar phantoms, respectively. These results are well within variations reported in the literature for these materials. It should be noted that phantom model stiffness can be heavily affected by the fabrication process and environmental conditions.

In order to apply this scheme to MIS, the OCT configuration should be a miniature probe type. In addition, precise robot control is required to compare the values measured at different sites because the indentation direction should be vertical to the tissue surface for accurate comparison. For *in-vivo* medical environments, the absolute displacement must be calculated by different refractive indexes of inhomogeneous biological tissues. However, as mentioned, a more critical factor, in this case, is to confirm the relative difference between normal and diseased tissues within the tissue. Hence, the tissue inhomogeneity is less affected.

V. Conclusion

In this study, an OCE system and a robotic system were used in conjunction to explore the feasibility of OCE stiffness mapping that can be batch-calibrated using information from the robot. We successfully demonstrated that the calibration could improve the final estimated strain for palpation. After calibration, the error decreased by 99% in silicon and 92% in agar. We also showed that OCE calibration may not be necessary across samples from the same material and that errors up to 20% in local strain may be present if the OCE algorithm is not re-calibrated across samples. The current work is limited in having a small sample size for different agar phantoms. A more robust exploration of error margins without recalibration of the OCE will be needed. Nevertheless, since the key point of OCE stiffness imaging is to discern spatial stiffness gradients, the exact value of Young's modulus is not critical. We believe that this is the first step toward a future application of OCE stiffness imaging/palpation using minimally invasive robots, and we will be working on integrating the OCE into a continuum robot in the future.

References

[1] P. Culmer, J. Barrie, R. Hewson, M. Levesley, M. Mon-Williams, D. Jayne, and A. Neville, "Reviewing the technological challenges associated with the development of a laparoscopic palpation device," *The International Journal of Medical Robotics and Computer Assisted Surgery*, vol. 8, no. 2, pp. 146–159, 2012.

[2] V. Egorov, S. Ayrapetyan, and A. Sarvazyan, "Prostate mechanical imaging: 3-d image composition and feature calculations," *IEEE Transactions on Medical Imaging*, vol. 25, no. 10, pp. 1329–1340, 2006.

[3] P. S. Wellman, E. P. Dalton, D. Krag, K. A. Kern, and R. D. Howe, "Tactile imaging of breast masses: first clinical report," *Archives of surgery*, vol. 136, no. 2, pp. 204–208, 2001.

[4] A. P. Miller, W. J. Peine, J. S. Son, and M. Z. T. Hammoud, "Tactile imaging system for localizing lung nodules during video assisted thoracoscopic surgery," in *Proceedings 2007 IEEE International Conference on Robotics and Automation*, 2007, pp. 2996–3001.

[5] A. S. Naidu, R. V. Patel, and M. D. Naish, "Low-cost disposable tactile sensors for palpation in minimally invasive surgery," *IEEE/ASME Transactions on Mechatronics*, vol. 22, no. 1, pp. 127–137, 2017.

[6] S. McKinley, A. Garg, S. Sen, R. Kapadia, A. Murali, K. Nichols, S. Lim, S. Patil, P. Abbeel, A. M. Okamura, and K. Goldberg, "A single-use haptic palpation probe for locating subcutaneous blood vessels in robot-assisted minimally invasive surgery," in *2015 IEEE International Conference on Automation Science and Engineering (CASE)*, 2015, pp. 1151–1158.

[7] I. B. Wanninayake, P. Dasgupta, L. D. Seneviratne, and K. Althoefer, "Air-float palpation probe for tissue abnormality identification during minimally invasive surgery," *IEEE Transactions on Biomedical Engineering*, vol. 60, no. 10, pp. 2735–2744, 2013.

[8] P. A. Patlan-Rosales and A. Krupa, "Robotic assistance for ultrasound elastography providing autonomous palpation with teleoperation and haptic feedback capabilities," in *2020 8th IEEE RAS/EMBS International Conference for Biomedical Robotics and Biomechatronics (BioRob)*, 2020, pp. 1018–1023.

[9] T. Yamamoto, B. Vagvolgyi, K. Balaji, L. L. Whitcomb, and A. M. Okamura, "Tissue property estimation and graphical display for teleoperated robot-assisted surgery," in *2009 IEEE International Conference on Robotics and Automation*, 2009, pp. 4239–4245.

[10] N. Shihora, R. Yasin, R. Walsh, and N. Simaan, "Feasibility of remote landmark identification for cricothyrotomy using robotic palpation," in *2021 IEEE/RSJ International Conference on Intelligent Robots and Systems (IROS)*, 2021, pp. 1808–1814.

[11] R. Yasin, P. Chalasani, N. Zevallos, M. Shahbazi, Z. Li, A. Deguet, P. Kazanzides, H. Choset, R. H. Taylor, and N. Simaan, "Evaluation of hybrid control and palpation assistance for situational awareness in telemanipulated task execution," *IEEE Transactions on Medical Robotics and Bionics*, vol. 3, no. 1, pp. 31–43, 2021.

[12] L. Anschuetz, M. Shelan, M. Dematté, A. D. Schubert, R. Giger, and O. Elicin, "Long-term functional outcome after laryngeal cancer treatment," *Radiation oncology*, vol. 14, no. 1, pp. 1–8, 2019.

[13] A. Bibas, A. G. Podoleanu, R. Cucu, M. Bonmarin, G. Dobre, V. Ward, E. Odell, A. Boxer, M. Gleeson, and D. A. Jackson, "3-d optical coherence tomography of the laryngeal mucosa," *Clinical Otolaryngology & Allied Sciences*, vol. 29, no. 6, pp. 713–720, 2004.

[14] A. Sepehr, W. B. Armstrong, S. Guo, J. Su, J. Perez, Z. Chen, and B. J. Wong, "Optical coherence tomography of the larynx in the awake patient," *Otolaryngology—Head and Neck Surgery*, vol. 138, no. 4, pp. 425–429, 2008.

[15] L. J. Lauwerends, H. A. Galema, J. A. Hardillo, A. Sewnaik, D. Monserez, P. B. van Driel, C. Verhoef, R. J. Baatenburg de Jong, D. E. Hilling, and S. Keereweer, "Current intraoperative imaging techniques to improve surgical resection of laryngeal cancer: a systematic review," *Cancers*, vol. 13, no. 8, p. 1895, 2021.

[16] G. D. Giudice, A. L. Orekhov, J.-H. Shen, K. M. Joos, and N. Simaan, "Investigation of micromotion kinematics of continuum robots for volumetric oct and oct-guided visual servoing," *IEEE/ASME Transactions on Mechatronics*, vol. 26, no. 5, pp. 2604–2615, 2021.

[17] D. C. Ghiglia and M. D. Pritt, "Two-dimensional phase unwrapping: theory, algorithms, and software," *A Wiley Interscience Publication*, 1998.

[18] F. G. Malheiro, "Towards clinical optical elastography: high-speed 3d imaging using volumetric phase detection," Ph.D. dissertation, 2014.

[19] V. Y. Zaitsev, S. Y. Ksenofontov, A. A. Sovetsky, A. L. Matveyev, L. A. Matveev, A. A. Zykov, and G. V. Gelikonov, "Real-time strain and elasticity imaging in phase-sensitive optical coherence elastography using a computationally efficient realization of the vector method," in *Photonics*, vol. 8, no. 12. MDPI, 2021, p. 527.

[20] K. V. Larin and D. D. Sampson, "Optical coherence elastography–oct at work in tissue biomechanics," *Biomedical optics express*, vol. 8, no. 2, pp. 1172–1202, 2017.
[21] Y. Hashimoto and Y. Monnai, "Noncontact estimation of stiffness based on optical coherence elastography under acoustic radiation pressure," in *2020 IEEE/RSJ International Conference on Intelligent Robots and Systems (IROS)*. IEEE, 2020, pp. 9840–9845.
[22] J. M. Schmitt, "Oct elastography: imaging microscopic deformation and strain of tissue," *Optics express*, vol. 3, no. 6, pp. 199–211, 1998.
[23] V. Y. Zaitsev, A. L. Matveyev, L. A. Matveev, A. A. Sovetsky, M. S. Hepburn, A. Mowla, and B. F. Kennedy, "Strain and elasticity imaging in compression optical coherence elastography: the two-decade perspective and recent advances," *Journal of biophotonics*, vol. 14, no. 2, p. e202000257, 2021.
[24] S. J. Kirkpatrick, R. K. Wang, and D. D. Duncan, "Oct-based elastography for large and small deformations," *Optics express*, vol. 14, no. 24, pp. 11 585–11 597, 2006.
[25] A. Nahas, M. Bauer, S. Roux, and A. C. Boccara, "3d static elastography at the micrometer scale using full field oct," *Biomedical optics express*, vol. 4, no. 10, pp. 2138–2149, 2013.
[26] V. Y. Zaitsev, A. L. Matveyev, L. A. Matveev, G. V. Gelikonov, V. M. Gelikonov, and A. Vitkin, "Deformation-induced speckle-pattern evolution and feasibility of correlational speckle tracking in optical coherence elastography," *Journal of biomedical optics*, vol. 20, no. 7, p. 075006, 2015.
[27] R. K. Wang, Z. Ma, and S. J. Kirkpatrick, "Tissue doppler optical coherence elastography for real time strain rate and strain mapping of soft tissue," *Applied Physics Letters*, vol. 89, no. 14, p. 144103, 2006.
[28] C. Song, M. Ahn, and D.-G. Gweon, "High resolution spectral domain optical coherence tomography with a broadband superluminescent diode laser source," in *Focus on Microscopy 2008*, 2008.
[29] C. Song, M. Ahn, and D. Gweon, "Polarization-sensitive spectral-domain optical coherence tomography using a multi-line single camera spectrometer," *Optics Express*, vol. 18, no. 23, pp. 23 805–23 817, 2010.
[30] B. F. Kennedy, S. H. Koh, R. A. McLaughlin, K. M. Kennedy, P. R. Munro, and D. D. Sampson, "Strain estimation in phase-sensitive optical coherence elastography," *Biomedical optics express*, vol. 3, no. 8, pp. 1865–1879, 2012.
[31] B. Dong, N. Huang, Y. Bai, and S. Xie, "Deep-learning-based approach for strain estimation in phase-sensitive optical coherence elastography," *Optics Letters*, vol. 46, no. 23, pp. 5914–5917, 2021.
[32] M. Al-Akhras, H. Ali, K. Aljarrah, A. Al-Omari, H. Al-Khateeb, B. Albiss, K. Azez, and G. Makhadmeh, "Influence of extremely low energy radiation on artificial tissue: Effects on image quality and superficial dose," *Spectroscopy*, vol. 22, no. 5, pp. 419–428, 2008.
[33] J. M. Walker, A. M. Myers, M. D. Schluchter, V. M. Goldberg, A. I. Caplan, J. A. Berilla, J. M. Mansour, and J. F. Welter, "Nondestructive evaluation of hydrogel mechanical properties using ultrasound," *Annals of Biomedical Engineering*, vol. 39, no. 10, pp. 2521–2530, 2011.